Processing and Application of Ceramics 18 [2] (2024) 172–179
https://doi.org/10.2298/PAC2402172G

Utilizing two-point correlation method for microstructure and mechanical evaluation of silicon nitride ceramics

Grzegorz Grabowski[1,*], Marek Grabowy[2,*], Agnieszka Wojteczko[1], Paweł Rutkowski[1], Zbigniew Pędzich[1]

[1]*AGH University of Krakow, Faculty of Materials Science and Ceramics, 30 Mickiewicza Av., 30-059 Krakow, Poland*
[2]*IEN Institute of Power Engineering, Ceramic Branch CEREL, 1 Techniczna St., 36-040 Boguchwała, Poland*

Received 27 March 2024; Received in revised form 17 May 2024; Accepted 6 June 2024

Abstract

In this article, the impact of microstructure on the mechanical properties of silicon nitride materials obtained by the liquid-phase sintering method was investigated. Using image analysis based on the two-point correlation method, the relationship between the autocorrelation length (ACL) parameter and the homogeneity of the microstructure and its impact on mechanical properties were examined. It was shown that lower ACL values, indicating greater microstructure homogeneity, correlate with better mechanical properties, such as bending strength, hardness and fracture toughness. The two-point correlation analysis demonstrated advantages over traditional microstructural analysis methods, offering efficiency, precision and automation capabilities, which are crucial for quality control in the industry.

Keywords: *two-point correlation method, Si_3N_4, microstructure, mechanical properties*

I. Introduction

Silicon nitride has been the subject of intensive research for several decades [1–7]. Its applications are now commercialized across various branches of technology, particularly as a component in machinery and devices subjected to high mechanical stresses, especially at elevated temperatures [8–12], where high chemical resistance [13,14] and superior tribological properties [15] are essential. As a fundamental requirement, the mentioned applications necessitate a high density of the sintered ceramics. For this purpose, sintering additives, predominantly in the form of oxides, are employed. Fundamental compositions comprise Y_2O_3 and Al_2O_3 [16,17]. However, research involving alternative additives, such as rare earth oxides [18,19], has demonstrated significant influences on the properties of the liquid phase during sintering, the grain growth process, and the attributes of the final sintered products.

To establish correlations between the composition parameters of the initial powder mixture, the technological parameters of the manufacturing process and the properties of the sintered materials, it is imperative to provide a precise description of the microstructures. Essential microstructural parameters, including the quantity of individual phases, pore volume and the size and morphology of grains, are typically assessed using stereological measurements conducted on polished cross-sections of samples, showing visible intergranular boundaries. Differentiation between individual phases is typically achieved through phase contrast (via electron backscattered diffraction methods, BSE) or chemical composition contrast (EDS). Such measurements are conducted with the resolution and precision afforded by scanning electron microscopy (SEM).

When observing samples with micron or submicron-sized features in the microstructure, accurately locating the grain boundary presents a methodological challenge. The use of a relatively broad electron beam, which collects signals from both the surface and the underlying layer, provides a signal that averages and blurs images of areas with different chemical composition. For silicon nitride, the microscopic image appears relatively dark due to its low average atomic mass, whereas the liquid phase, enriched with yttrium or other dense rare earth elements, emits an intensely bright signal. Accurately delineating

*Corresponding author: tel: +48 12 617 25 06
e-mail: *grzegorz.grabowski@agh.edu.pl; grabowy@cerel.pl*

the boundary between silicon nitride grains and the liquid phase is not always feasible with straightforward imaging techniques like secondary electron diffraction (SE). This technique provides a precise signal from the surface but loses information regarding the phase compositions. There are available techniques that enable the collection of precise signals from the surface; however, such detection methods (e.g. BSE Optic LAM) are only available with the latest microscope models.

In this work, we discuss a less commonly utilized image analysis method employing two-point correlation, facilitating rapid analysis of standard SEM images, assessment of fundamental microstructural parameters of sintered materials and their correlation with critical material properties for application purposes, including density, bending strength, fracture toughness, Young's modulus and hardness.

II. Experimental

2.1. Sample preparation

Two commercial silicon nitride powders: Si_3N_4 Grade M11 (>90% α-Si_3N_4) and Si_3N_4 Grade B7 (>87% α-Si_3N_4) both from H.C. Starck, Germany, as well as Y_2O_3 (>99.999%, Xiguanya Mining Industry Co. Ltd, China), Al_2O_3 (>99.0%, TM Dar, Taimicron Co. Ltd, Japan) and Yb_2O_3 (>99.99%, Qingdao Xiguanya Mining Industry Co. Ltd, China) were used for sample preparation. The silicon nitride M11 and B7 powders had different average grain sizes and specific surfaces, i.e. 0.6 μm/12–15 m^2/g and 1.1 μm/6 m^2/g, respectively. Mixing of the starting powders was conducted using different methods, including ball, gravity, and rotary-vibration milling. Mixing and homogenization times and the types of used grinding media were different: zirconia or silicon nitride. The granulation method was also varied, i.e. a spray dryer and sieve granulation were used. Table 1 lists the compositions of the mixtures and the basic parameters of the homogenization conditions used for the powder mixtures prepared in this work. The symbols 5Y, 5A and 1Yb indicate the content of oxide additives in the masses, i.e. 5 wt.% of Y_2O_3, 5 wt.% of Al_2O_3 and 1 wt.% of Yb_2O_3.

Mixtures of powders were isostatically pressed under 250 MPa in mould, having length of 60 mm, width of 10 mm and high of 8 mm. Sintering process was conducted in an electrical furnace in nitrogen atmosphere at pressure of 100 bar. Basic parameters were 100 °C/min heating rate up to maximum temperature of 1785 °C with 90 min soaking time.

2.2. Sample characterization

The apparent density and water absorption rates of the samples were ascertained through hydrostatic weighing in water. Sintering shrinkage was calculated by measuring the lengths of the bars pre- and post-sintering. Phase composition of the sintered ceramics was characterized by X-ray diffraction (XRD, Empyrean/Malvern Panalytical by using Cu-K_α radiation). Microstructural images were obtained by examining polished cross-sectional surfaces with a Thermo Scientific Scios 2 (US) electron microscope, equipped with an EDS analyser. The samples were not etched and carbon was sprayed onto the surface to improve the conductivity of the sample.

The Young's modulus of the sintered materials was calculated using the speed of ultrasonic wave propagation through the material. The ultrasonic flaw detector Olympus Epoch 650 (Olympus, Japan) which complied with the EN12668-1 standard [20] was used. Bending strength and fracture toughness were assessed employing the three-point bending method. The bars described in the sample preparation chapter were bent. Notched beams were used to determine the fracture toughness. A Zwick/Roell Z020 (Germany) machine was used. Bars were tested using 3-point bending test with support width of 40 mm. Hardness measurements were conducted with the Vickers method, utilizing the FuturTech hardness tester FV-700 (Japan). An indenter load of 10 N was applied for 10 s.

Table 1. Characteristic technological parameters of investigated samples

Sample	Additives [wt.%]	Type of Si_3N_4 powder	Milling time [h]	Type of mill / grinding media	Granulation
A	5 Y_2O_3 5 Al_2O_3	100% B7	0.5	Atrittor / ZrO_2	On sieve
B	5 Y_2O_3 5 Al_2O_3	100% M11	0.5	Atrittor / ZrO_2	On sieve
C	5 Y_2O_3 5 Al_2O_3	25% B7 – 75% M11	0.5	Atrittor / ZrO_2	On sieve
D	5 Y_2O_3 5 Al_2O_3	100% M11	3	Ball mill / Si_3N_4	Spray dryer
E	5 Y_2O_3 5 Al_2O_3	100% B7	3	Ball mill / Si_3N_4	Spray dryer
F	4 Y_2O_3 5 Al_2O_3 1 Yb_2O_3	100% M11	0.5	Atrittor / ZrO_2	On sieve

2.3. Two-point correlation method

Image analysis was conducted using the two-point correlation method, which facilitates the examination of various spatial relationships, including the distribution of grains, pores, or other microstructure features. This was achieved by assessing the variability in the probability of an element's occurrence relative to the distance from a reference point [21]. The method is grounded in the determination of a specific probability distribution function, $P_2(r)$, known as the two-point autocorrelation function, which is dependent on the distance, r. This function calculates the likelihood that two points, separated by a distance r, reside within the area occupied by a chosen phase (α). In the case of a microstructure without long-range order (fully stochastic microstructure), for the distance between the points $r = 0$, the probability is equal to the volume fraction V_V of the α phase in the material $V_V = A_A$ and, with increasing the distance between the points, it quickly decreases to the value close to V_V^2 ($P_2(r) = V_V^2$) when $r \to \infty$. However, if the distribution of phases in the material is not completely random and there is at least a slight order (e.g. agglomeration), the values of the P_2 function decrease more slowly with the distance r and, additionally, this function may have local maxima. Such a complex shape of the $P_2(r)$ function indicates the presence of long-distance correlation (order) in the microstructure. Hence, the autocorrelation function's shape is indicative of a particular microstructure, encapsulating information about grain sizes and their spatial arrangement [22–24].

Autocorrelation length (ACL) is a key parameter in the two-point correlation analysis, gauging the correlation decay rate between points, thus serving as an indicator of the microstructure's randomness [23,25]. If the $P_2(r)$ function exhibits no clear oscillations, the ACL can be approximated as the distance at which the autocorrelation function's value nears the theoretical value (V_V^2) with the adopted tolerance threshold δ ($ACL = r$, when $V_V(r) = \delta \cdot (V_V - V_V^2) + V_V^2$).

In this study, we employed the aforementioned method to determine the ACL, setting the tolerance threshold δ at 0.05. Furthermore, to facilitate a direct comparison of the two-point autocorrelation function shapes across various sample series (which have differing volume fractions of the α phase), we normalized the variability range to span from 1 to 0. This normalization corresponds to the fluctuation between V_V and V_V^2. The normalizing function used for this purpose was:

$$f_2(r) = \frac{P_2(r) - V_V^2}{V_V - V_V^2} \tag{1}$$

Matlab-based computational procedure was employed to ascertain the two-point autocorrelation function and the subsequent autocorrelation distance for all analysed images. The computational script processed binary images as input data, which were obtained systematically and repeatably using predefined processing parameters. First, the dimensions in pixels were determined for each image. Then, from the range of these dimensions, the coordinate values of the first point were drawn and based on them the coordinates of the second point were calculated, with an assumed radius r and a random direction. If the coordinate values of the second point were outside the range of image dimensions, their values were corrected. Periodic boundary conditions were applied for any necessary corrections. For each pair of points, represented by binary image pixels, the procedure read their brightness values (0 or 1) to check for correlation. A correlation was assumed if the brightness values for both points matched and corresponded to the brightness of the analysed phase α. Otherwise, the points were deemed uncorrelated. In this way, by repeating the procedure for subsequent pairs of points, information was collected and allowed the determination of the correlation probability at the assumed radius r. This probability was computed using the equation:

$$P_2 = \frac{n_c}{n} \tag{2}$$

where n_c represents the number of point pairs meeting the correlation criterion, and n denotes the total number of point pairs assessed for correlation. For this analysis, we consistently used a constant value of $n = 10^6$, applied across various radius values and all binary images. The procedure was executed iteratively for radius r values ranging from 1 pixel to a distance equivalent to 1 μm. Figure 1 illustrates an example graph of the two-point correlation function as a function of radius r.

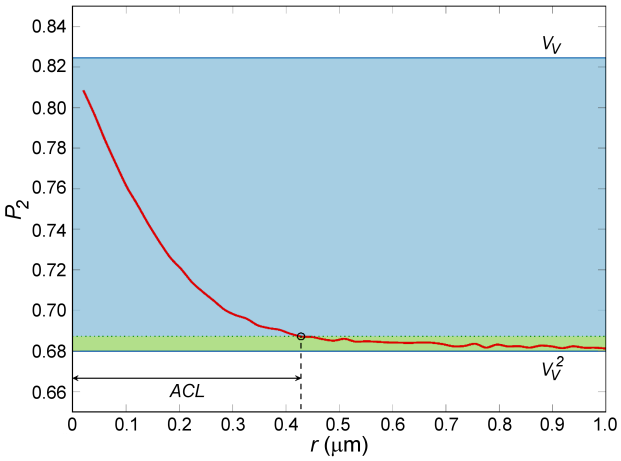

Figure 1. An illustration of the two-point correlation function $P_2(r)$ and indication of ACL (the area under the tolerance threshold δ is marked in green)

Beyond the two-point correlation method applied for microstructure analysis, we also determined characteristic dimensions for the largest grain population observed in the SEM images. For the selected grains (usually 2–3 grains in each image), we measured the following dimensions: c, representing the length along the grain's long axis, and a, denoting the width at the grain's broad-

Table 2. Physical and mechanical properties of investigated samples: apparent density (ρ), shrinkage on firing ($\Delta l/l$), ultrasonic wave velocity (v), Young's modulus (E), bending strength (σ), fracture toughness (K_{IC}), hardness (Hv)

Sample	ρ [g/cm^3] ±0.01	$\Delta l/l$ [%] ± < 0.05%	v [m/s] ± < 0.1%	E [GPa]	σ [MPa]	K_{IC} [MPa m$^{0.5}$]	Hv [GPa]
A	3.24	16.62	10837	381 ± 4	537 ± 61	5.55 ± 0.17	13.23 ± 0.47
B	3.24	16.33	11057	396 ± 5	665 ± 80	6.72 ± 0.12	14.04 ± 0.36
C	3.24	16.50	10337	346 ± 5	539 ± 53	6.56 ± 0.21	13.24 ± 0.41
D	3.23	16.52	10557	360 ± 6	673 ± 65	6.21 ± 0.14	13.68 ± 0.32
E	3.23	16.76	10428	336 ± 7	593 ± 132	5.97 ± 0.45	13.83 ± 0.29
F	3.26	16.37	10917	369 ± 4	560 ± 101	6.04 ± 0.10	13.95 ± 0.37

est point, perpendicular to c. In this way, a dozen measurements of the lengths of the characteristic dimensions a and c were collected for each of the materials analysed.

III. Results and discussion

Table 2 provides a summary of the physical and mechanical properties of the tested samples. The data demonstrate how the choice of silicon nitride powder, technological parameters and oxide additives significantly influence the resulting properties of the nitride material. All investigated samples have 100% of β-Si_3N_4 phase. As an example, XRD pattern of the sintered sample is presented in Fig. 2. XRD patterns for all investigated materials were almost identical. Sintering additives formed the amorphous phase, which was not visible in XRD patterns.

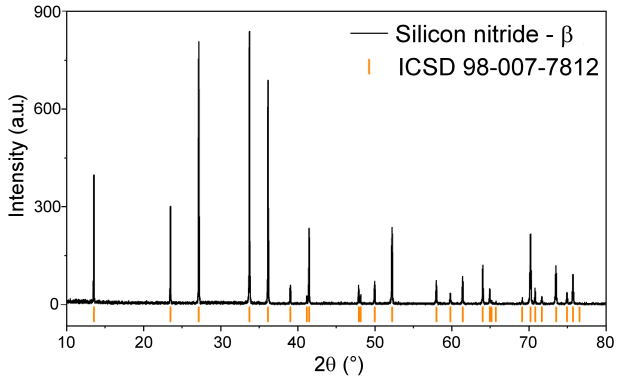

Figure 2. Example XRD pattern for the obtained Si_3N_4 samples

According to the presented results it can be concluded that differences in mechanical properties came from microstructural differences which were a consequence of applied manufacturing procedures on the level of powder preparation. Pressing and sintering conditions were the same for all samples.

All tested materials nominally containing 10% sintering additives, predominantly comprising 5% each of Y_2O_3 and Al_2O_3. In just one sample, 1% of Y_2O_3 was substituted with Yb_2O_3. Microstructural observations of the sintered materials are shown in Figs. 3–8. There are differences in the amount and distribution of porosity, the amount of liquid phase and the size and shape of grains. Despite these differences, the microstructures exhibit notable similarities. Typically, these include both crystalline and amorphous phases, with the latter having two forms: elongated and isometric, which are quite similar to each other. When comparing these images with the physical and mechanical property values, it is challenging to ascertain at first glance which microstructures correlate with superior or inferior material properties.

Table 3 summarizes the measured characteristic lengths c and a, for grains observed in the SEM images. Analysis of these values indicates that optimal mechanical properties are associated with grains that are neither excessively long nor overly slender. The samples B, D and E exhibit the most favourable length-to-width ratios (c/a) demonstrating moderate elongation (c). The samples A and C, which possess the most elongated grains, exhibit the poorest mechanical performance. From the perspective of fracture mechanics, this correlation is logical, as the largest grains represent the most significant potential defects within the microstructure. The samples F have the highest value of c/a ratio, but due to the small thickness (a) of the highly elongated grains (slender grains) their effect on mechanical properties is negligible. The samples from this series obtain average values for all measured mechanical parameters.

It is important to mention that the aforementioned correlations do not extend to Young's modulus and hardness values. Theoretically, the speed of wave propagation within the material and its hardness should strongly correlate with its degree of compaction. The conducted tests reveal that the materials are non-absorbent, meaning they lack open porosity and exhibit similar densification levels, with differences amounting to only 0.1 g/cm^3 (the sample with ytterbium must have a slightly higher theoretical density due to the density of ytterbium oxide). This suggests that all samples should exhibit similar ultrasonic wave transmission and hardness. However, this is not observed, particularly when comparing the samples D and E. These are materials made according to the same technological procedure from different sources of nitride powders. They have identical density and similar microstructural parameters, but clearly differ in all mechanical parameters. In this case, analysing basic microstructural parameters, like the values of c and a, does not reveal differences

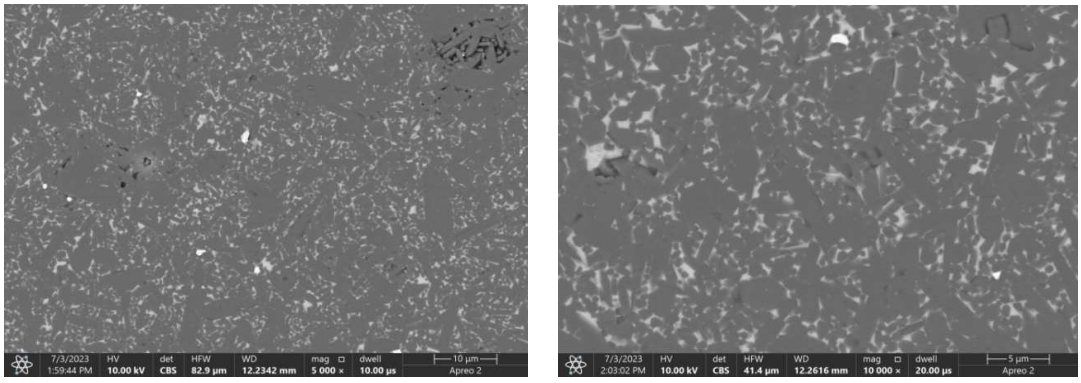

Figure 3. Typical SEM microstructures of the sample A at different magnifications: 5,000× (left) and 10,000× (right)

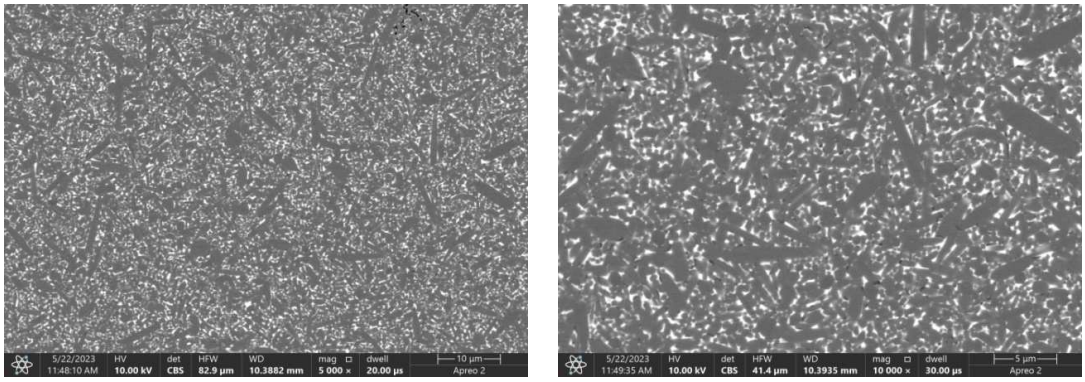

Figure 4. Typical SEM microstructures of the sample B at different magnifications: 5,000× (left) and 10,000× (right)

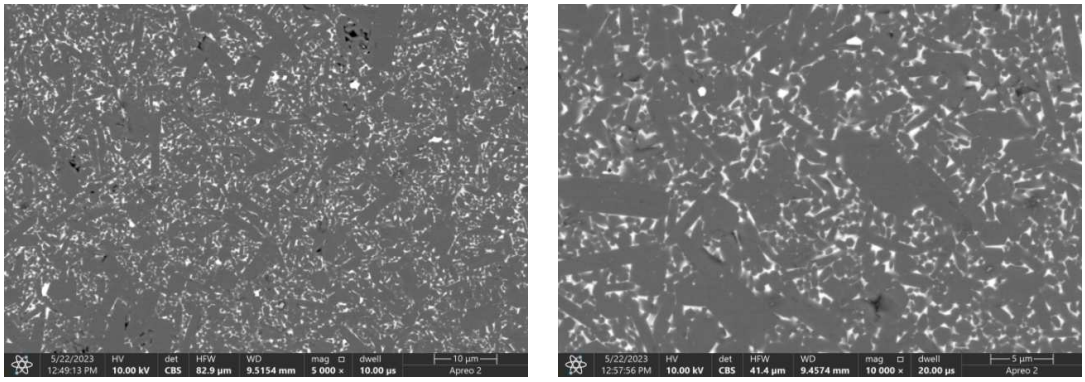

Figure 5. Typical SEM microstructures of the sample C at different magnifications: 5,000× (left) and 10,000× (right)

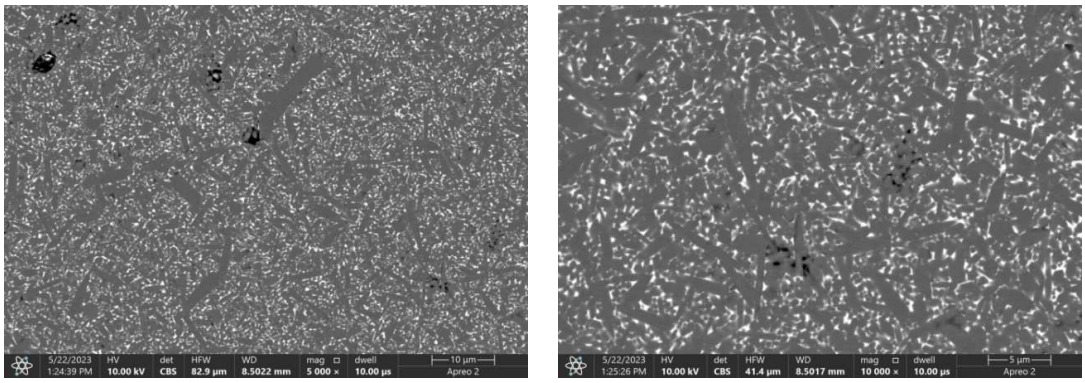

Figure 6. Typical SEM microstructures of the sample D at different magnifications: 5,000× (left) and 10,000× (right)

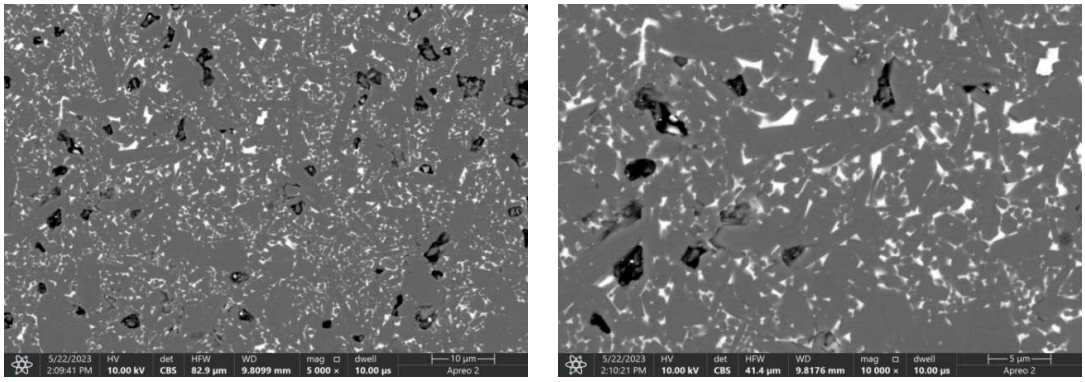

Figure 7. Typical SEM microstructures of the sample E at different magnifications: 5,000× (left) and 10,000× (right)

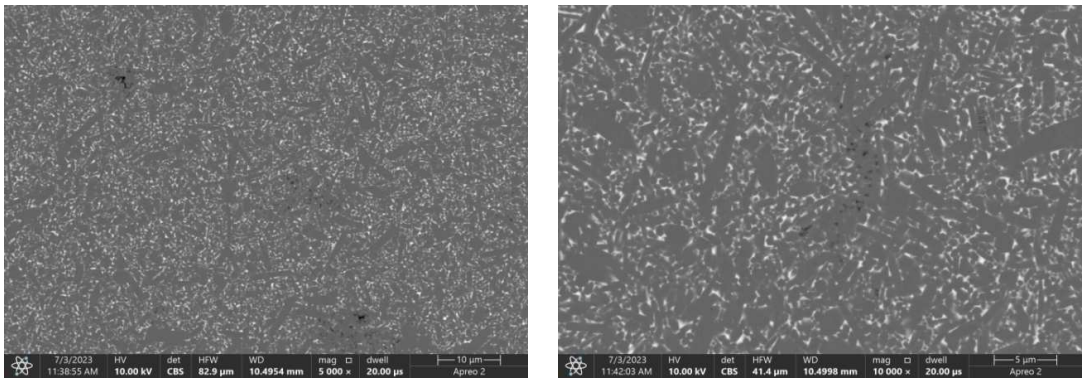

Figure 8. Typical SEM microstructures of the sample F at different magnifications: 5,000× (left) and 10,000× (right)

Table 3. Results of grain size measurements

Sample	Size in c dimension [μm]	Size in a dimension [μm]	c/a ratio
A	13.3 ± 1.9	2.6 ± 0.7	5.1 ± 0.6
B	7.1 ± 0.9	1.4 ± 0.2	5.1 ± 0.7
C	13.3 ± 2.2	3.4 ± 0.6	3.9 ± 1.8
D	9.3 ± 1.2	1.2 ± 0.3	7.8 ± 1.6
E	9.2 ± 0.4	1.1 ± 0.4	8.4 ± 0.7
F	8.7 ± 1.3	1.0 ± 0.2	8.7 ± 1.3

in the properties of these materials. Nevertheless, significant microstructural differences are apparent in the two-point correlation curves.

For the sample B, the *ACL* value is notably low, as indicated in Table 4, with only the sample F exhibiting a marginally lower *ACL*. This low *ACL* value signifies a swift loss of point-to-point correlation, implying a highly homogeneous microstructure. This microstructural homogeneity prevents local stress concentrations (with minimal local thermal stress values [26]) and reduces the scattering of ultrasonic waves on inhomogeneities. Consequently, this sample exhibited the highest determined value of Young's modulus. Moreover, the microstructural homogenization positively influences other mechanical properties, such as bending strength, hardness, and crack resistance, all of which are highest for the sample B.

On the other hand, for the sample E, the *ACL* value is the highest among the analysed materials, more than twice as high as that of the sample B. This indicates that the point-to-point correlation persists over a much larger area, suggesting greater microstructural heterogeneity. Consequently, despite having a favourable c/a ratio, indicative of optimal Si_3N_4 grain shape, the sample E exhibited significantly inferior mechanical properties compared to the sample B.

The samples A and C exhibit *ACL* value nearly twice as high as those of the sample B. Consequently, this higher *ACL* value may account for the notably inferior mechanical properties of the samples A and C compared to the sample B.

In contrast, the F samples have the smallest c/a ratio value and therefore have the most homogenized microstructure. Despite this, due to the unfavourable c/a ratio (grains too elongated), no improvement in mechanical properties was noted in this series.

IV. Conclusions

The presented results offer a new perspective on the relationship between microstructure and the mechanical properties of silicon nitride materials. We have tried to

Table 4. Calculated *ACL* parameter values

Sample	*ACL*, magnification SEM 5000× [μm]	*ACL*, magnification SEM 10000× [μm]	Mean value *ACL* [μm]
A	0.667 ± 0.001	0.667 ± 0.003	0.667 ± 0.002
B	0.389 ± 0.001	0.333 ± 0.014	0.361 ± 0.028
C	0.556 ± 0.039	0.694 ± 0.039	0.625 ± 0.058
D	0.389 ± 0.001	0.389 ± 0.001	0.389 ± 0.001
E	0.833 ± 0.001	0.806 ± 0.005	0.819 ± 0.025
F	0.389 ± 0.032	0.333 ± 0.016	0.361 ± 0.038

compare series of samples derived from different starting powders which were treated in a different way at the stage of powder preparation. The forming process and sintering conditions were the same for all investigated samples. It assured that observed mechanical differences came directly from the microstructural differences of samples.

By employing image analysis based on the two-point correlation method, more precise characterization of the microstructure, enhancing our understanding of its impact on the material's mechanical properties was achieved. The findings suggest that the autocorrelation length (*ACL*) parameter can be a useful indicator for assessing the homogeneity of the microstructure, allowing for effective differentiation of samples with similar microstructures. It was observed that variations in *ACL* values correlate with different mechanical properties, underscoring the importance of quantitative microstructural analysis. The two-point correlation analysis proved particularly valuable for silicon nitride materials, where conventional analysis methods faced challenges due to low interphase contrast. Moreover, this method offers automation potential, which could be beneficial for quality control in the industry.

In conclusion, the conducted research validates the significance of quantitative microstructural analysis in evaluating and predicting the mechanical properties of silicon nitride materials, which could contribute to improvements in manufacturing processes and quality control in the materials sector.

Acknowledgements: Project was financed by the National Centre for Research and Development (NCBR), grant "Innovative material on the base of silicon nitride with extremely high thermal shock resistance, strength and corrosion resistance" No. POIR.01.01.01-00-0102/21 Fast track. The SEM investigations were supported by the program Excellence Initiative - Research University for the AGH University of Krakow, Grant ID 1449.

References

1. N.L. Parr, G.F. Martin, E.R.W. May, "Preparation, microstructure and mechanical properties of silicon nitride", pp. 102–135 in *Special Ceramics*. Ed. P. Popper, Heywood, London, UK, 1960.
2. F.F. Lange, "Relation between strength, fracture energy and microstructure of hot-pressed Si_3N_4", *J. Am. Ceram. Soc.*, **56** [10] (1973) 518–552.
3. M.H. Lewis, R.J. Lumby, "Nitrogen ceramics: Liquid phase sintering", *Powder Metall.*, **26** (1983) 73–81.
4. R.N. Katz, G.D. Quinn, "Time-temperature effects in nitride and carbide ceramics", pp. 491-501 in *Progress in Nitrogen Ceramics*, Ed. F.L. Riley, Martinus Nijhoff, The Hague, 1983.
5. I.-W. Chen, P.F. Becher, M. Mitomo, G. Petzow, T.-S. Yen, *Silicon Nitride Ceramics: Scientific and Technological Advances*, Materials Research Society, Pittsburgh, PA, 1993**.**
6. F.L. Riley, "Silicon nitride and related materials", *J. Am. Ceram. Soc.*, **83** [2] (2004) 245–265.
7. R.F. Coe, "Silicon nitride products", *British Patent No. 1092637*, 1967.
8. S. Hampshire, "Silicon nitride ceramics", in *Engineered Ceramics: Current Status and Future Prospects*. Eds. T. Ohji, M. Singh, American Ceramic Society, Westerville, OH, 2016.
9. Y. Zhou, H. Hyuga, D. Kusano, Y. Yoshizawa, K. Hirao, "A tough silicon nitride ceramic with high thermal conductivity", *Adv. Mater.*, **23** [39] (2011) 4563–4567.
10. H. Klemm, "Silicon nitride for high-temperature applications", *J. Am. Ceram. Soc.*, **93** (2010) 1501–1522.
11. M. Tatarková, P. Tatarko, P. Šajgalík, "Si_3N_4 Ceramics, Structure and Properties", pp. 109-118 in *Encyclopedia of Materials: Technical Ceramics and Glasses*, Vol. 2. Ed. M. Pomeroy, Elsevier, Oxford, 2021.
12. K. Hirao, K. Watari, H. Hayashi, M. Kitayama, "High thermal conductivity silicon nitride ceramics", *MRS Bulletin*, **26** (2001) 451–455.
13. N.S. Jacobson, "Corrosion of silicon-based ceramics in combustion environments", *J. Am. Ceram. Soc.*, **76** [1] (1993) 3–28.
14. D. Galusková, M. Kašiarová, M. Hnatko, D. Galusek, J. Dusza, P. Šajgalík, "Hydrothermal corrosion and flexural strength of Si_3N_4-based ceramics", *Corrosion Sci.*, **85** (2014) 94–100.
15. A.C. Lee, H.-H. Lu , H.-T. Lin, P. Šajgalík , D.-F. Lii, Pramoda, K. Nayak, C.-Y. Chen, J.-L. Huang, "Nanopowder processing of ultrafine Si_3N_4 with improved wear resistance", *J. Asian Ceram. Soc.*, **3** (2015) 6–12.
16. H.-H. Lu, Ch.-Y. Chen, "Investigation of nano-silicon nitride ceramics containing an yttria sintering additive and the carbon thermal reduction reaction", *Ceram. Int.*, **42** (2016) 12452–12459.
17. C.C. Ye, H.Q. Ru, Z.B. Qin, S.W. Zhao, H.S. Jia, D.L. Chen, "Silicon nitride composites with magnesia and alumina additives: Toughening mechanisms and mechanical properties", *Mater. Sci. Eng. A*, **779** (2020) 139140.
18. P. Tatarko, Š. Lojanová, J. Dusza, P. Šajgalík, "Influence of various rare-earth oxide additives on microstructure and mechanical properties of silicon nitride based nanocomposites", *Mater. Sci. Eng. A*, **527** [18-19] (2010) 4771–4778.
19. W. Liu, W. Tong, W. Lu, S. Wu, "Effects of different

types of rare earth oxide additives on the properties of silicon nitride ceramic substrates", *Ceram. Int*., **45** [9] (2019) 12436–12442.
20. Non-destructive testing - Characterization and verification of ultrasonic test equipment - Part 1: *Instruments, European Standard* EN ISO 22232-1:2021.
21. S. Torquato, *Random Heterogeneous Materials* (Interdisciplinary Applied Mathematics), Springer New York, NY, 2002.
22. P.-E. Chen, W. Xu, N. Chawla, Y. Ren, Y. Jiao, "Hierarchical n-point polytope functions for quantitative representation of complex heterogeneous materials and microstructural evolution", *Acta Mater*., **179** (2019) 317–327.
23. C.A. Falchetto, K.H. Moon, "A novel micromechanical-analogical model for low temperature creep properties of asphalt binder and mixture", *Canad. J. Civil Eng*., **42** [12] (2015) 1019–1031.
24. M.A. Ioannidis, M.J. Kwiecien, I. Chatzis, "Statistical analysis of the porous microstructure as a method for estimating reservoir permeability", *J. Petroleum Sci. Eng*., **16** [4] (1996) 251–261.
25. Y. Zhang, S. Sundararajan, "Generating random surfaces with desired autocorrelation length", *Appl. Phys. Lett*., **88** [14] (2006) 16–19.
26. A. Dubiel, G. Grabowski, M. Goły, S. Skrzypek, "The influence of thermal residual stresses on mechanical properties of silicon nitride-based composites", *Materials*, **13** [5] (2020) 1092–1114.